

# JGR Solid Earth

## RESEARCH ARTICLE

10.1029/2023JB028332

### Key Points:

- A new crustal model with much more reliable and denser *Pms* anisotropic measurements is built in the eastern Tibetan Margin
- Songpan-Ganzi Block is likely deformed by crustal shortening and lower crustal flow
- Channel flow may exist in the west low velocity zone (LVZ) while absent at the east LVZ

### Supporting Information:

Supporting Information may be found in the online version of this article.

### Correspondence to:

Y. Zheng,  
zhengyong@cug.edu.cn

### Citation:

Zeng, S., Niu, F., Sun, Y., Ai, S., Wang, S., & Zheng, Y. (2024). Crustal structure and anisotropy measured by CHINArray and implications for complicated deformation mechanisms beneath the eastern Tibetan margin. *Journal of Geophysical Research: Solid Earth*, 129, e2023JB028332. <https://doi.org/10.1029/2023JB028332>

Received 29 NOV 2023







Accepted 7 JUN 2024

### Author Contributions:

**Conceptualization:** Sijia Zeng, Fenglin Niu, Ya Sun, Yong Zheng  
**Data curation:** Sijia Zeng, Fenglin Niu, Sixue Wang  
**Formal analysis:** Sijia Zeng, Fenglin Niu  
**Funding acquisition:** Yong Zheng  
**Methodology:** Fenglin Niu, Ya Sun  
**Resources:** Yong Zheng  
**Software:** Sijia Zeng, Fenglin Niu, Ya Sun, Sanxi Ai  
**Validation:** Sanxi Ai  
**Visualization:** Sijia Zeng, Fenglin Niu  
**Writing – original draft:** Sijia Zeng, Fenglin Niu  
**Writing – review & editing:** Fenglin Niu, Ya Sun, Sanxi Ai, Sixue Wang, Yong Zheng

© 2024. American Geophysical Union. All Rights Reserved.

## Crustal Structure and Anisotropy Measured by CHINArray and Implications for Complicated Deformation Mechanisms Beneath the Eastern Tibetan Margin

Sijia Zeng<sup>1,2</sup> , Fenglin Niu<sup>3</sup> , Ya Sun<sup>4</sup> , Sanxi Ai<sup>1,2</sup> , Sixue Wang<sup>1,2</sup> , and Yong Zheng<sup>1,2</sup> 

<sup>1</sup>Hubei Subsurface Multi-Scale Imaging Key Laboratory, School of Geophysics and Geomatics, China University of Geosciences, Wuhan, China, <sup>2</sup>State Key Laboratory of Geological Processes and Mineral Resources, School of Geophysics and Geomatics, China University of Geosciences, Wuhan, China, <sup>3</sup>Department of Earth, Environmental and Planetary Sciences, Rice University, Houston, TX, USA, <sup>4</sup>School of Geosciences and Info-Physics, Central South University, Changsha, China

**Abstract** We investigated velocity and anisotropic structure of the crust beneath the eastern margin of the Tibetan Plateau to better understand its deformation and evolution mechanism. We performed *H-κ* and *Pms* anisotropy analyses to obtain crustal thickness, *Vp/Vs* ratio, fast polarization direction, and splitting time from 711 stations, and further conducted quality control using slowness, harmonic and statistical analyses. The Songpan-Ganzi Block has a large splitting time and a fast polarization direction roughly parallel to the GPS motion and SKS fast direction. It also shows an overall high but complex distribution of *Vp/Vs* ratio, and large variations in crustal thickness, indicating that crustal deformation is likely caused by crustal shortening and lower crustal flow. The northern Sichuan-Yunnan Rhombic Block (SYRB) is featured by a thick crust and high *Vp/Vs* ratio, suggesting that the crust is likely inflated by partial melting lower crustal rocks. The subblock also exhibits a strong azimuthal anisotropy with a splitting time greater than 0.6 s. The fast polarization direction aligns with the nearly N-S extended direction and rotates clockwise in front of the Emeishan Large Igneous Province (ELIP). The observed anisotropy agrees with aligned amphibole minerals under a simple shear condition, supporting a southward lower crust flow being diverted by the ELIP. Anisotropy measurements on the southern SYRB are less robust and widely scattered, suggesting a deformation mechanism different from the northern SYRB. In addition, the southeastern margin of the Sichuan Basin shows a systematic pattern of crustal anisotropy consistent with a pure shear deformation mechanism.

**Plain Language Summary** We studied the crustal structure and deformation beneath the eastern edge of the Tibetan Plateau. By analyzing teleseismic data from 727 stations, we measured crust thickness, *Vp/Vs* ratio, and azimuthal anisotropy using receiver functions. Our findings show a complex crustal behavior pattern in the eastern Tibet margin. In the Songpan-Ganzi Block, crustal shortening and lower crust flow seem to be causing deformation. The northern Sichuan-Yunnan Rhombic Block, with its thick crust and high *Vp/Vs* ratio, appears to be influenced by partial melting of lower crust rocks. And a southward lower crust flow being diverted by the Emeishan Large Igneous Province. The eastern and southern part of this block shows a different pattern, indicating a unique deformation mechanism. Additionally, the southeastern margin of the Sichuan Basin appears to undergo a distinct type of crustal deformation.

## 1. Introduction

The Tibetan Plateau, primarily formed by the India-Asia collision beginning around 50 Ma, has been the forefront of studying collision tectonics and continental deformation. Laboratory experiment (Tapponnier et al., 1982) suggested that the collision displaced Indochina and South China by hundreds of kilometers to the southeast and east, respectively. Numerical study of England and Houseman (1986) indicated that crustal thickening and lateral displacement of the plateau can be generally explained by a thin viscous sheet model with an indenting boundary condition. While it is certain that the formation of the plateau is related to the collision, many details on the evolution of the plateau are yet to be answered (Yin & Harrison, 2000). Whether the plateau has simply displaced like “extrusion of blocks” (Tapponnier et al., 1982, 1990) or has been growing over time (e.g., Clark et al., 2005), is still debated. The east margin of the Tibetan Plateau, which includes the Songpan-Ganzi Block (SGB) in the north and the Sichuan Yunnan Rhombic Block (SYRB) in the south (Figure 1), is an ideal place to address questions of whether and how the plateau expands due to large amount field data available in this area.

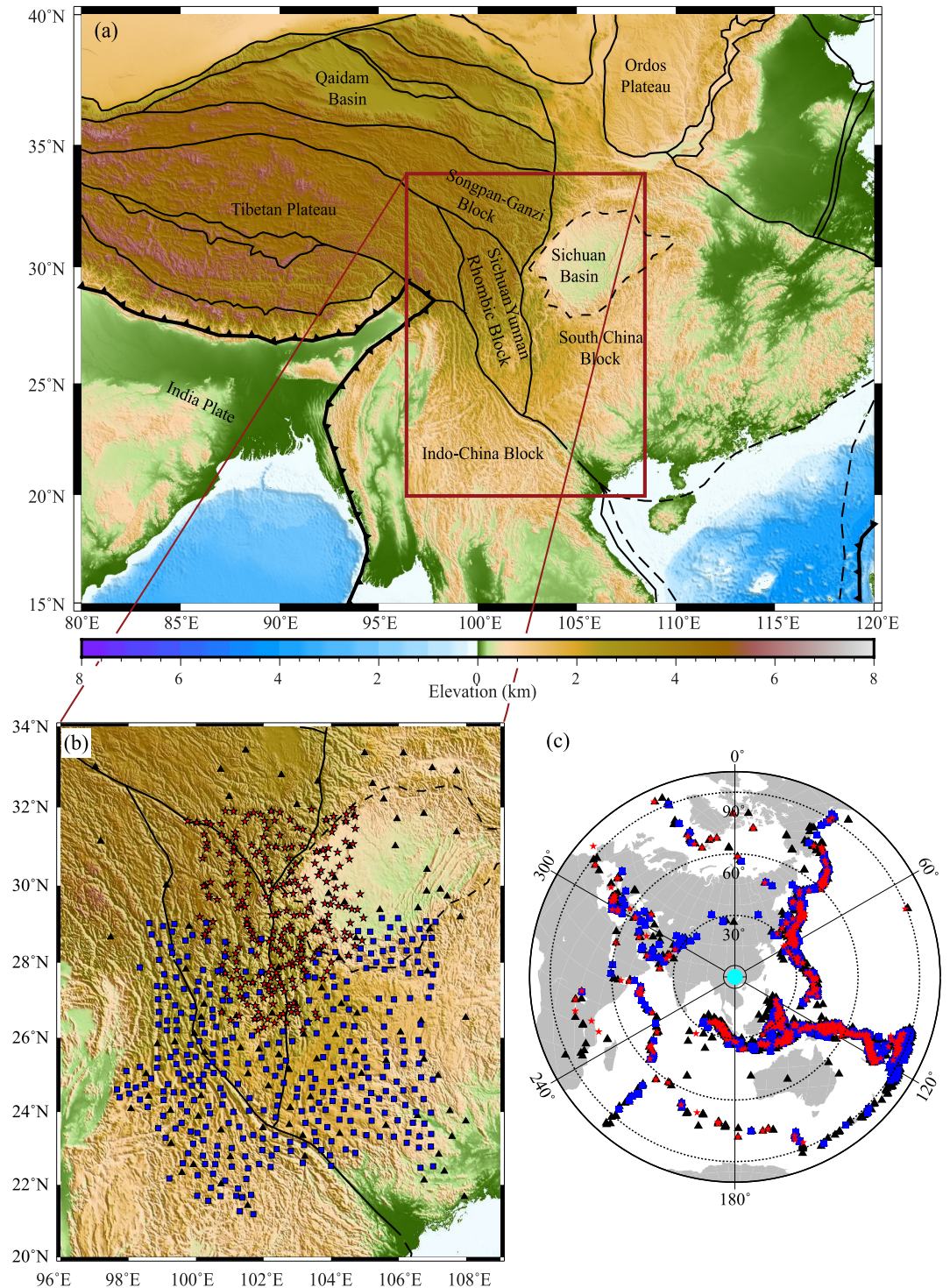


**Figure 1.** (a) Topographic map showing the eastern margin of the Tibetan Plateau and its surrounding areas. Black lines indicate boundaries of plates and tectonic blocks. (b) Topographic map showing the location of the 297 CHINArray-T1 (stars), 350 CHINArray-X1 (squares), and 80 CEArray (triangles) broadband stations. (c) Azimuthal equidistant map showing the 3,071 earthquakes used in computing receiver functions with symbols corresponding to the arrays shown in (b). The solid cyan circle at the center indicates the array center, roughly located at 27°N and 102°E. Note that although some events fall within the 30° circle or beyond the 90° from the array center, all the seismograms that we used have an epicenter distance between 30° and 90°.

Based on topographic relief data and numerical modeling, Clark and Royden (2000) proposed a channel flow model that explains the eastward expansion of the plateau through flows of lower crustal materials from central Tibet to the margin. The lower crustal flow inflates the crust at the margins, leading to the lateral expansion of the plateau. Growth directions depend on rheology of the surrounding crust as the flow tends to avoid the strong Sichuan Basin and moves around it laterally. Flows toward the northern and southern edges of the Sichuan Basin experienced less resistance, resulting in a low topographic gradient in the northeastern (NE) and southeastern (SE) margins of the plateau. The flow toward east is almost blocked by the Sichuan Basin, which caused a steep topographic gradient at the eastern margin of the plateau. The lower crustal model is, however, not supported by geological data from the Longmenshan (LMS) range at the eastern edge of the plateau and its front (Hubbard & Shaw, 2009), which suggest that crustal shortening is the primary driver for the uplift of the LMS range. Hu et al. (2022) conducted isotopic analyses of the igneous rocks at the eastern Tibet-Gongga-Zheduo Massif and found that the rocks are derived from partial melting of the local crust of SGB, instead of a distinct crust carried by a lower crust flow from the central plateau.

Over the last two decades, numerous geophysical investigations have been conducted to find the evidence of the lower crustal flow with distinct seismic and electrical properties. C. Wang et al. (2003) conducted P- and S-wave tomography of the eastern margin with traveltimes data from local and regional earthquakes and found pervasive low-velocity anomalies that are unevenly distributed and connected to major fault zones. Due to the low station density in the area as well as the limited ability of traveltimes tomography in imaging low-velocity structures, the lateral resolution of early traveltimes tomography is relatively low. Recent deployment of the CHINArray and incorporation of ambient noise data, together with the improvement in seismic tomography have led to high resolution images of the crust beneath the eastern margin (e.g., Bao et al., 2015; Y. Liu et al., 2023; Shen et al., 2016; Y. Yang et al., 2020; X. Yang et al., 2023; Zhang et al., 2020). All the tomographic models showed a large scale low-velocity anomaly beneath the SGB, which extends southward to the northern part of the SYRB. A separate low velocity anomaly is present at the southeastern tip of the SYRB and extends to the southwestern part of the South China Block (SCB). Zhao et al. (2013) conducted Lg-wave Q tomography and found that low-Q anomalies overlap well with the lower velocity zones. Magnetotelluric imaging also showed two lower crustal channels with high electrical conductivity that extend from the Tibetan Plateau into southwest China (Bai et al., 2010). It seems that the two channels are split by the Emeishan Large Igneous Province (ELIP) (X. Li et al., 2020). It should be noted that the two channel flows inferred from magnetotelluric data are based on interpolations of 2-D images. Therefore, whether the high electrical conductivity bodies imaged by 2-D profiles are connected or not is still questionable.

The low velocity, high attenuation, and high electrical conductivity have been interpreted partial melts with an elevated fluid content. We notice that both tomographic and magnetotelluric images capture the static properties (i.e., seismic velocity and electrical conductivity) of the crust. A lower crust with low seismic velocity, high attenuation, and high electrical conductivity does not necessarily mean a channel flow. Seismic anisotropy, on the other hand, is a property associated with rock deformation, and thus can be used complementarily to image crustal or mantle flow.

J. Xie et al. (2017) inverted surface wave data for a 3-D anisotropic model of the eastern Tibetan plateau and found a steeply dipping tilted hexagonally symmetric (THS) upper crustal medium overlying a shallowly dipping THS medium in the middle-to-lower crust beneath the plateau. This may suggest a decoupled deformation between the upper and lower crust. Within the southeastern part of the plateau, the observed fast polarization direction in the lower crust aligns generally with the flow direction proposed by Clark and Royden (2000). At the periphery of the plateau, the anisotropic medium is steeply dipping throughout the entire crust, which could arise from either overall crustal shortening at the margins or a redirection of lower crustal flow after encountering significant resistance at the forefront. Bao et al. (2020) conducted a surface wave tomography with ambient noise data to develop a detailed 3-D anisotropic model of the eastern Tibetan Plateau and its neighboring regions. The model revealed limited azimuthal anisotropy in the lower crust beneath SGB and SYRB except for the eastern margin of the plateau, where the lower crust exhibits a prominent azimuthal anisotropy with the fast direction parallel to the margin's strike. The observation does not seem support the lower crustal flow model. In general, discerning the lower crustal model remains challenging with anisotropic models inverted from surface wave data, partly because there is a tradeoff between propagation anisotropy and velocity heterogeneity. This tradeoff can be mitigated by using S wave splitting, which is influenced by polarization anisotropy.

Sun et al. (2012) measured crustal thickness,  $V_p/V_s$  ratio, and crustal anisotropy using 79 permanent broadband stations in the SE Tibet operated by the China Earthquake Administration (CEArray). They found that the crust beneath SYRB has a thickness of  $\sim 50\text{--}70$  km and a  $V_p/V_s$  ratio of  $\sim 1.79$ . The relatively high  $V_p/V_s$  ratio is employed to argue that crust beneath the SE Tibet might have been thickened by addition of mafic lower crust rocks. Sun et al. (2012) was able to obtain only 12 measurements of crustal anisotropy, which indicate that the lower crust beneath SYRB is strongly anisotropic (6%) with a fast polarization direction parallel to the lower crustal flow direction proposed by Clark and Royden (2000). Q. Wang et al. (2016) conducted a similar investigation using CEArray stations on the northeastern margin of the plateau and found that the fast polarization is nearly perpendicular to the proposed lower crust flow direction, which led them to conclude that there is a lack of lower crust flow beneath the northeastern margin.

As the P-to-S converted phase at the Moho ( $Pms$ ) on individual receiver functions (RFs) is of low signal-to-noise ratio (SNR), it is very challenging to robustly extract crustal anisotropy from  $Pms$  data. This may explain why each of the above two studies (Sun et al., 2012; Q. Wang et al., 2016) was able to obtain only 12 measurements from several tens of CEArray stations even with more than 3 years of RF data. Therefore, the lateral resolution of these CEArray based anisotropic models is very limited, usually in the order of hundreds of kilometers. Thus, these low-resolution models can't be used to undoubtedly determine whether there are continuous outward flows in the lower crust beneath the eastern margin of the plateau. The deployment of CHINArray in the area provided an opportunity to build high-resolution crustal anisotropy models of the study area. In fact, multiple studies have been conducted to measure crustal anisotropy using  $Pms$  of teleseismic events recorded by the CHINArray (e.g., Cai et al., 2016; Han et al., 2020; Peng et al., 2022; T. Zheng et al., 2018). All the studies showed large variations in both the fast polarization direction ( $\varphi$ ) and splitting time ( $\delta t$ ). The averaged splitting time measured from stations on the plateau are much larger than that from stations in the surrounding areas. The scattered measurements and large discrepancy among different studies suggested that large errors might be present in measuring azimuthal anisotropy from  $Pms$  due to its low SNR. More specifically, the measurements can be also affected by a dipping Moho and lateral heterogeneities inside the crust.

Motivated to obtain high-resolution and accurate models of the eastern margin of the Tibetan plateau, to bridge the information gap between deformations in the crust and mantle, and to achieve a deeper understanding of the existence of channel flow, we utilize the dense spatial coverage of the temporary arrays (CHINArray-T1 and CHINArray-X1) and the long-term observation data of the CEArray. After strict quality control of raw and RF data, we estimate the crustal thickness,  $V_p/V_s$  ratio, and crustal anisotropy of the eastern Tibetan margin using RF data. We performed the slowness, harmonic and statistical analyses of  $Pms$  to ensure robust measurements of crustal anisotropy. By comparing our measurements with SKS splitting data and high-resolution 3-D velocity model, we strive to constrain the primary deformation mechanism at different parts of the margin.

## 2. Data and Analyses

### 2.1. CEArray, CHINArray-X1, and CHINArray-T1

To obtain a high-resolution model of crustal anisotropy beneath the eastern margin of the Tibetan plateau ( $21^\circ\text{N}\text{--}33.5^\circ\text{N}$ ,  $97^\circ\text{E}\text{--}108^\circ\text{E}$ ), we collected teleseismic records from a total of 727 broadband stations (Figure 1b) operated by the China Earthquake Administration (CEA), among which are 80 permanent CEArray stations, 297 CHINArray-T1 (also known as the West Sichuan array) and 350 CHINArray-X1 stations (also referred to as the CHINArray Phase I). The CEArray consists of a backbone national seismograph network (CNDSN), 31 regional networks, and several small aperture arrays with more than 1,000 stations (X. Zheng et al., 2009). Sun et al. (2012) used the similar CEArray stations and built a low-resolution ( $>100$  km) crustal anisotropy model of the study area. T1 and X1 are two different phases of the CHINArray project, which aims to cover mainland China with a rolling seismic array of 400–800 broadband sensors with a station spacing of 30–40 km and a deployment period of 18–36 months.

To generate RFs, we selected teleseismic events with a moment magnitude greater than 5.5 and an epicentral distance of  $30^\circ\text{--}90^\circ$  with respect to the stations. We obtained records of 3,071 teleseismic events from CEArray stations due to its long operation period (since middle of 2007). The number of teleseismic events from the two temporal networks are 654 (CHINArray-T1, 2006–2009) and 746 (CHINArray-X1, 2011–2013), respectively. Figure 1c shows the spatial distribution of teleseismic events, which provide a very good coverage in both epicentral distance and back-azimuthal directions. Niu and Li (2011) found a few CEArray stations had

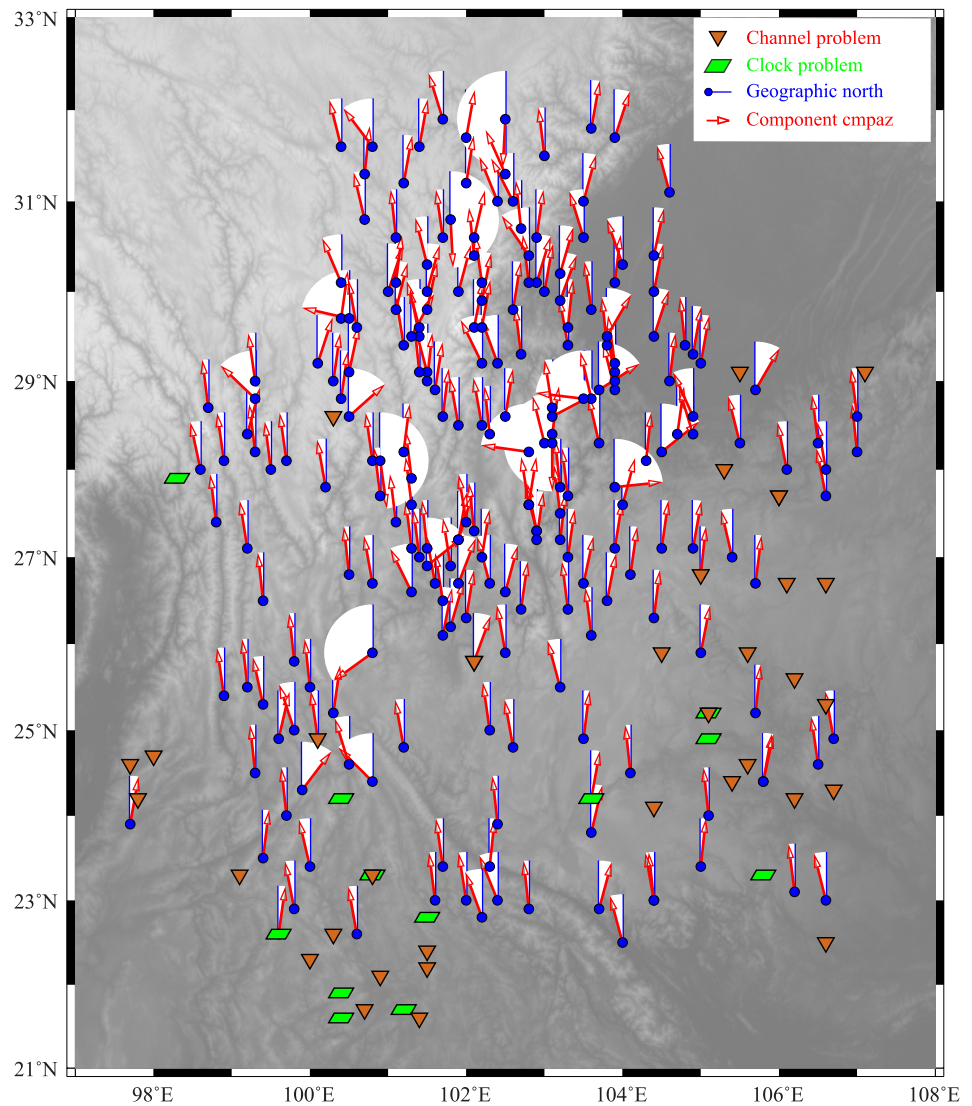


**Figure 2.** Map showing the 264 stations with a misalignment angle  $>5^\circ$  or other malfunctioning issues. Parallelograms indicate stations with a clock timing drifting, and inverted triangles represent stations with at least one component that had some glitches over part or the entire period of deployment. Solid circles indicate stations with a  $5^\circ +$  N-component azimuth, as indicated by the open arrows.

orientation issues in early days and developed a method to correct sensor misalignments. Zeng et al. (2020) applied the method to the CHINArray-X1 and found 129 stations had been misaligned by more than  $5^\circ$  or suffered other malfunctioning issues. We also applied the same analysis to the CHINArray-T1 stations and found 135 stations had a misorientation of more than  $5^\circ$  (Figure 2). The measured azimuth of the N-component of the CHINArray-T1 stations is listed in Table S1 in Supporting Information S1. In addition, 16 stations had other issues, such as timing, glitches, and dead channels (Figure 2), and therefore were excluded in further analyses. In summary, we selected 711 stations to compute RFs for estimating crustal thickness,  $V_p/V_s$  ratio, and crustal anisotropy. These stations form a dense array with a spacing of  $\sim 35$  km in an area of  $22^\circ\text{N}$ – $32^\circ\text{N}$  and  $98^\circ\text{E}$ – $108^\circ\text{E}$ .

## 2.2. Receiver Functions

We first rotated the two horizontal components of teleseismic records to the radial (R) and transverse (T) components based on the measured component azimuth and backazimuthal direction of the source-receiver great circle raypath. We further projected the vertical (Z) and radial components (R) to the principal directions of their

covariance matrix, known as the longitudinal (P) and in-plane transverse (SV) directions. We anticipated that the P-SV projection is more efficient in separating P- and S-wave energy than the Z-R projection (Niu et al., 2007). We employed the “water-level” deconvolution technique (Clayton & Wiggins, 1976) to generate R-, T-, and SV-component RFs. The Z-component was used as the source for computing R- and T-component RFs, while the P-component was deconvolved to produce the SV-component RFs. We set the water level to 0.01 and the Gaussian lowpass filter parameter to 1.5, which is equivalent to a corner frequency of ~0.5 Hz. We used both R and SV RFs in the  $H$ - $\kappa$  analysis, R and T RFs in estimating crustal anisotropy. We visually inspected all the R RFs and removed those with low SNR or other issues. The number of RFs selected is above 800 for a CEArray station and 200 for a CHINArray station.

### 2.3. $H$ - $\kappa$ Analysis

We employed the improved  $H$ - $\kappa$  method of Niu et al. (2007), which introduced a coherence index of the coda waves,  $c(\kappa)$ , into the calculation:

$$s(H, \kappa) = \frac{c(\kappa)}{(w_1 + w_2 + w_3)} \frac{1}{K} \sum_{i=1}^K \{w_1 r_i [t_{0p1s}(H, k)] + w_2 r_i [t_{2p1s}(H, k)] - w_3 r_i [t_{1p2s}(H, k)]\} \quad (1)$$

Here  $H$  and  $\kappa$  denote crustal thickness and  $V_p/V_s$  ratio, respectively.  $K$  is the total number of RFs,  $r_i[t]$  represents the  $i$ -th receiver function at the specified time,  $t$ . Following the notation of Niu and James (2002), we used  $npms$  to refer a later arrival, which travels in the crust with  $n$  P-wave and  $m$  S-wave legs. Consequently,  $t_{0p1s}$  denotes the arrival time of the primary  $Pms$  phase, while  $t_{2p1s}$  and  $t_{1p2s}$  represent the arrival times of the two reverberations.  $w_1$ ,  $w_2$ , and  $w_3$  are the weights assigned to the  $Pms$  and the two reverberations, which were set to 0.5, 0.25, and 0.25, respectively. We stacked the R- and SV-component RFs separately in searching for the maximum amplitude in the  $H$ - $\kappa$  domain. Furthermore, we performed three distinct stackings using the three later arrivals: (a) all the three phases, (b)  $0p1s$  and  $1p2s$ , and (c)  $0p1s$  and  $2p1s$ . Consequently, this process generated a total of six  $H$ - $\kappa$  results, comprising three from R RFs and three from SV RFs. Subsequently, we manually selected the result with the smallest uncertainties, typically favoring the SV stack of all the three phases.

The arrival times of the P to S converted phase and the two reverberations,  $t_{0p1s}$ ,  $t_{2p1s}$ , and  $t_{1p2s}$ , can be computed from crustal thickness ( $H$ ),  $V_p/V_s$  ratio ( $\kappa$ ), P-wave velocity of the crust ( $V_p$ ), and P-wave ray parameter ( $p$ ):

$$T_{0p1s} = T_{Pms} \cong H \left\{ \sqrt{\left(\frac{\kappa}{V_p}\right)^2 - p^2} - \sqrt{\left(\frac{1}{V_p}\right)^2 - p^2} \right\} \quad (2a)$$

$$T_{2p1s} \cong H \left\{ \sqrt{\left(\frac{\kappa}{V_p}\right)^2 - p^2} + \sqrt{\left(\frac{1}{V_p}\right)^2 - p^2} \right\} \quad (2b)$$

$$T_{1p2s} \cong 2H \left\{ \sqrt{\left(\frac{\kappa}{V_p}\right)^2 - p^2} \right\} \quad (2c)$$

Here the approximation arises from the fact that the Moho conversion ( $0p1s$ ) and the two multiples ( $2p1s$  and  $1p2s$ ) travel with ray parameters slightly different from that of the direct P wave. In fact, the former has a negative while the latter two have a positive slowness with respect to the direct P wave. We employed the 3-D crustal model, CRUST 1.0 (Laske et al., 2013), to compute average P-wave velocity beneath each station,  $V_p$ , and the 1-D iasp91 model (Kennett & Engdahl, 1991) to calculate the P-wave ray parameter,  $p$ .

We varied  $H$  from 20 to 70 km in increments of 0.1 km, and  $\kappa$  from 1.5 to 2.0 in increments of 0.001 to search the maximum value of  $s(H, \kappa)$ . If the above search couldn't lead to a well-defined peak, we manually adjusted the search ranges, which resulted in high  $V_p/V_s$  ratio (>2.0) and crustal thickness (>70 km) at some stations. Two examples of the  $H$ - $\kappa$  grid search at the CEArray station, SC.LTA, and CHINArray station, X1.53075, are shown in Figures 3a and 3b, respectively. Both stations exhibit a well-defined peak in the ( $H, \kappa$ ) domain due to the large number of RFs used in the stacking. We further stacked the RFs along a positive and a negative slowness to

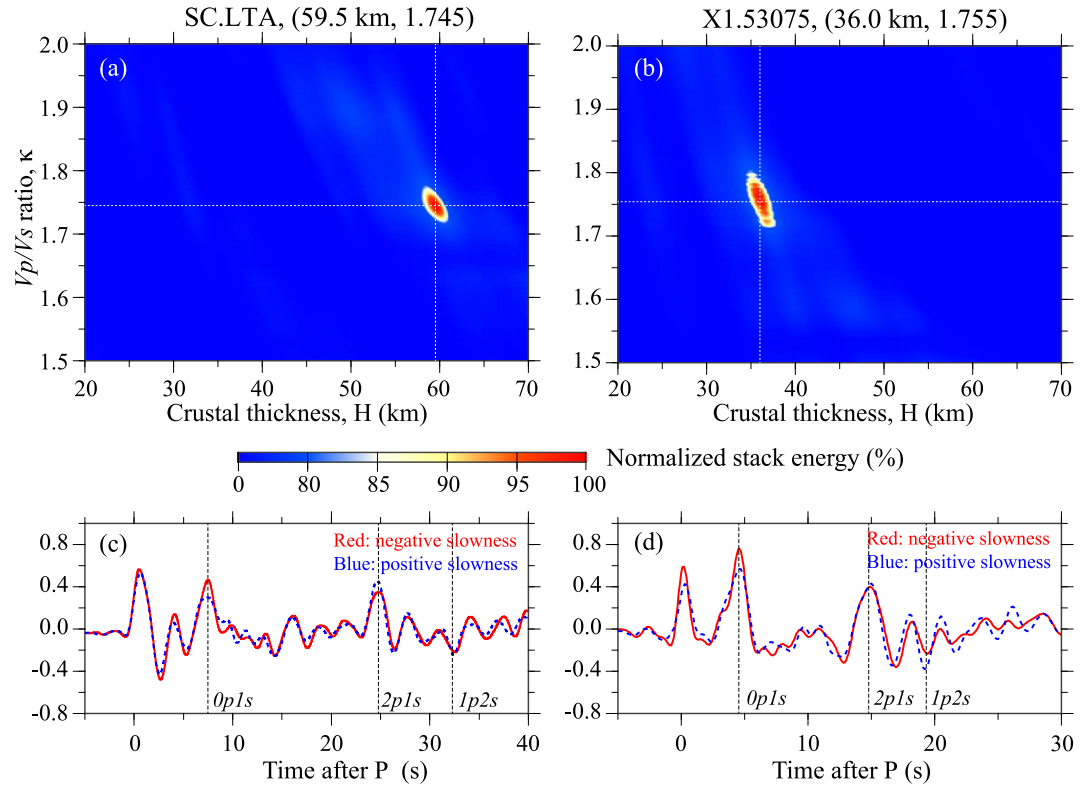


**Figure 3.** (a) and (b) are the  $H$ - $\kappa$  grid-search results using receiver functions recorded at stations SC.LTA and X1.53075, respectively. The contour of the stacking amplitude of the three lateral arrivals is shown as a function of crustal thickness (horizontal) and  $V_p/V_s$  ratio (vertical). The location of the amplitude peak is indicated by the two white lines. (c) and (d) show the time-domain stacked receiver functions with a negative slowness ( $P_{ms}$ , red solid line) and positive slowness (multiples, blue dashed line). Note that the amplitude of the phases is larger when they are stacked with the correct slowness.

confirm that  $0p1s$  is peaked at a negative slowness while  $2p1s$  and  $1p2s$  have larger amplitude at a positive slowness.

#### 2.4. Harmonic Analysis of the $P_{ms}$ Arrival Time

We employed radial (R) and tangential (T) RFs to estimate azimuthal anisotropy of the crust based on systematic variations of  $P_{ms}$  arrival time and waveform along the back-azimuthal direction. To do so, we first corrected the time moveouts related to epicentral distance. We used the  $H$ - $\kappa$  results to calculate the  $P_{ms}$  arrival time of each RFs ( $T_{P_{ms}}^i$ ) and a hypothetical receiver function with an epicentral distance of  $60^\circ$  and a source depth of 0 km ( $T_{P_{ms}}^r$ ). The arrival time differences of  $P_{ms}$  ( $\Delta T_{P_{ms}}^i = T_{P_{ms}}^i - T_{P_{ms}}^r$ ) are used as corrections to align all the RFs as if each one had an epicentral distance of  $60^\circ$  and a source depth of 0 km. We further normalized the R and T RFs by dividing them with the peak amplitude of the P wave on the R component.

We adopted the harmonic analysis of the corrected  $P_{ms}$  arrival times ( $T_{P_{ms}}^{i'} = T_{P_{ms}}^i - \Delta T_{P_{ms}}^i$ ) developed by Sun et al. (2012). For an assumed  $n$ -degree harmonic, we first computed the theoretical  $P_{ms}$  arrival time for each station:

$$T_{P_{ms}}^{n,i}(\theta_i) = T_{P_{ms}}^r + \frac{\delta t_n}{2} \cos \{n(\theta_i - \varphi_n)\} \quad (3)$$

Here  $\theta_i$  is the backazimuth of the  $i$ -th RF;  $\delta t_n$  and  $\varphi_n$  are the peak-to-peak amplitude and initial phase of the  $n$ -degree overtone. We then stacked R RFs along the theoretical traveltime curve. We varied  $\delta t_n$  from 0.0 to 1.5 s with increments of 0.02 s,  $\varphi_n$  from  $0^\circ$  to  $359^\circ$  with an increment of  $1^\circ$ . From all the  $(\delta t_n, \varphi_n)$  pairs, we searched the maximum amplitude ( $A_{n,max}$ ) and the maximum energy ( $E_{n,max}$ ) of stacked RFs, as well as the

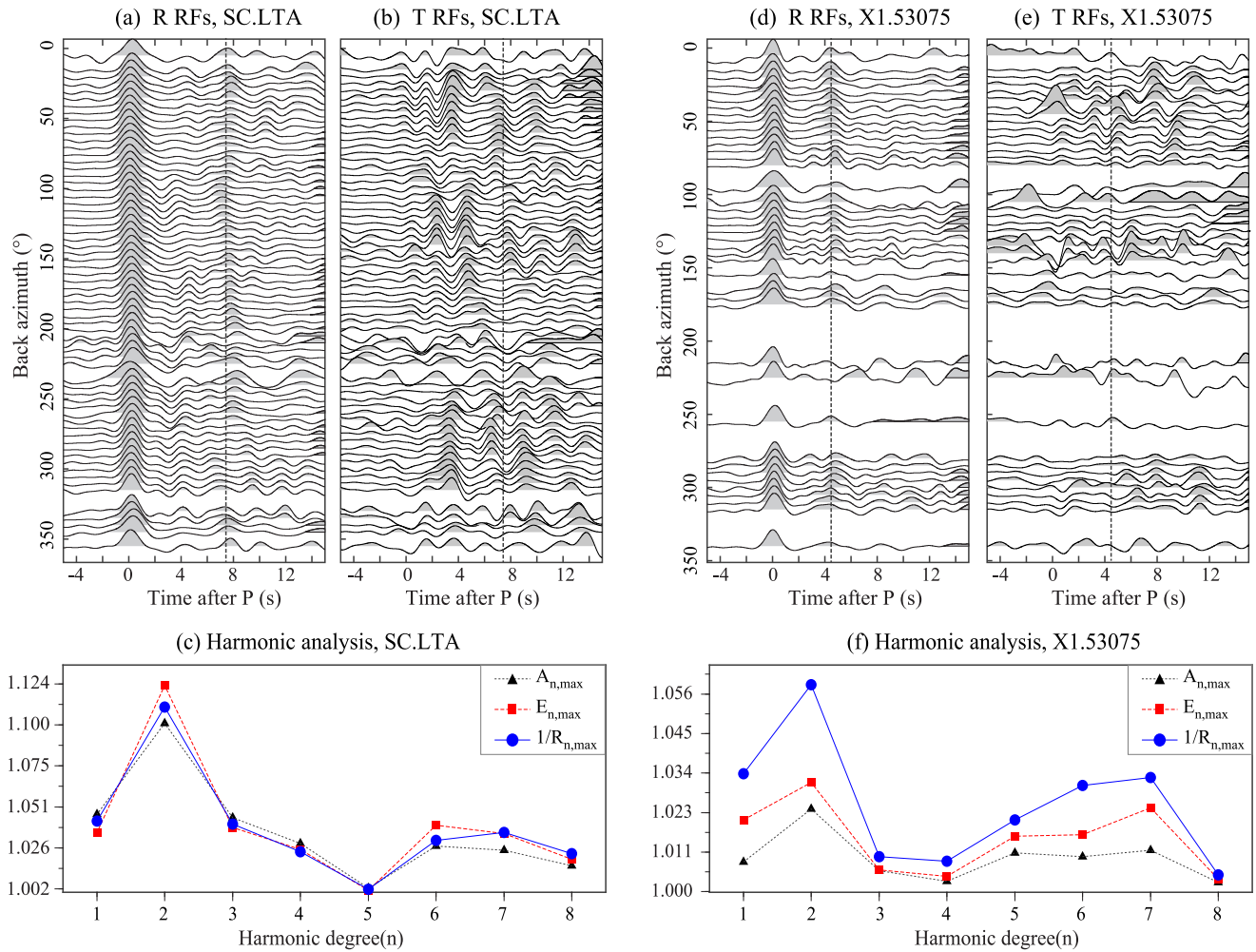


**Figure 4.** (a) and (b) show the R and T receiver functions recorded at station SC.LTA, plotted as a function of back azimuth. The receiver functions here are stacked in  $10^\circ$  bins along the back azimuth direction. Solid lines indicate the average  $Pms$  arrival time. (c) Results of the harmonic analysis at SC.LTA. The maximum value of peak amplitude and total energy, as well as the reciprocal of the minimum residual, are shown as a function of the harmonic degree. Note that they all reach their peak at harmonic degree 2, indicating that the observed azimuthal variations of  $Pms$  on receiver functions are primarily caused by azimuthal anisotropy. Note that the harmonic analysis also exhibits other types of azimuthal variations. (d–f) are the same as (a–c) except for station X1.53075.

minimum residual between the stacked and individual RFs ( $R_{n,min}$ ). They were further normalized by their corresponding values when  $\delta t_n = 0.0$  s. We computed the first 8 overtones ( $n = 1, 2, \dots, 8$ ) to examine patterns in  $T^i_{Pms}(\theta)$ . Lateral heterogeneities of S-wave velocity inside the crust and Moho topography, as well as seismic anisotropy, can lead to  $Pms$  azimuthal variations. For example, a dipping Moho or a crust with tilted transverse isotropy (TTI) is expected to produce a degree-1 harmonic variation (e.g., Levin & Park, 1997; Savage, 1998). A degree-2 harmonic is usually caused by an anisotropic crust with a horizontal transverse isotropy (HTI) structure. Small-scale anomalies, on the other hand, may cause higher degree variations. The harmonic analysis results at stations SC.LTA and X1.53075 are shown in Figure 4. Both stations exhibit a dominant degree-2 harmonic, an indicative of an HTI crust beneath these two stations. Numerous studies have demonstrated that a dipping Moho can induce azimuthal variations in the arrival time of  $Pms$  waves, as well as variations in energy observed on the transverse component. Notably, these azimuthal variations often exhibit a discernible degree-1 pattern (H. Liu & Niu, 2012; Q. Wang et al., 2016). Consequently, we only chose stations that exhibit a dominant degree-2 harmonic for crustal anisotropy measurement.



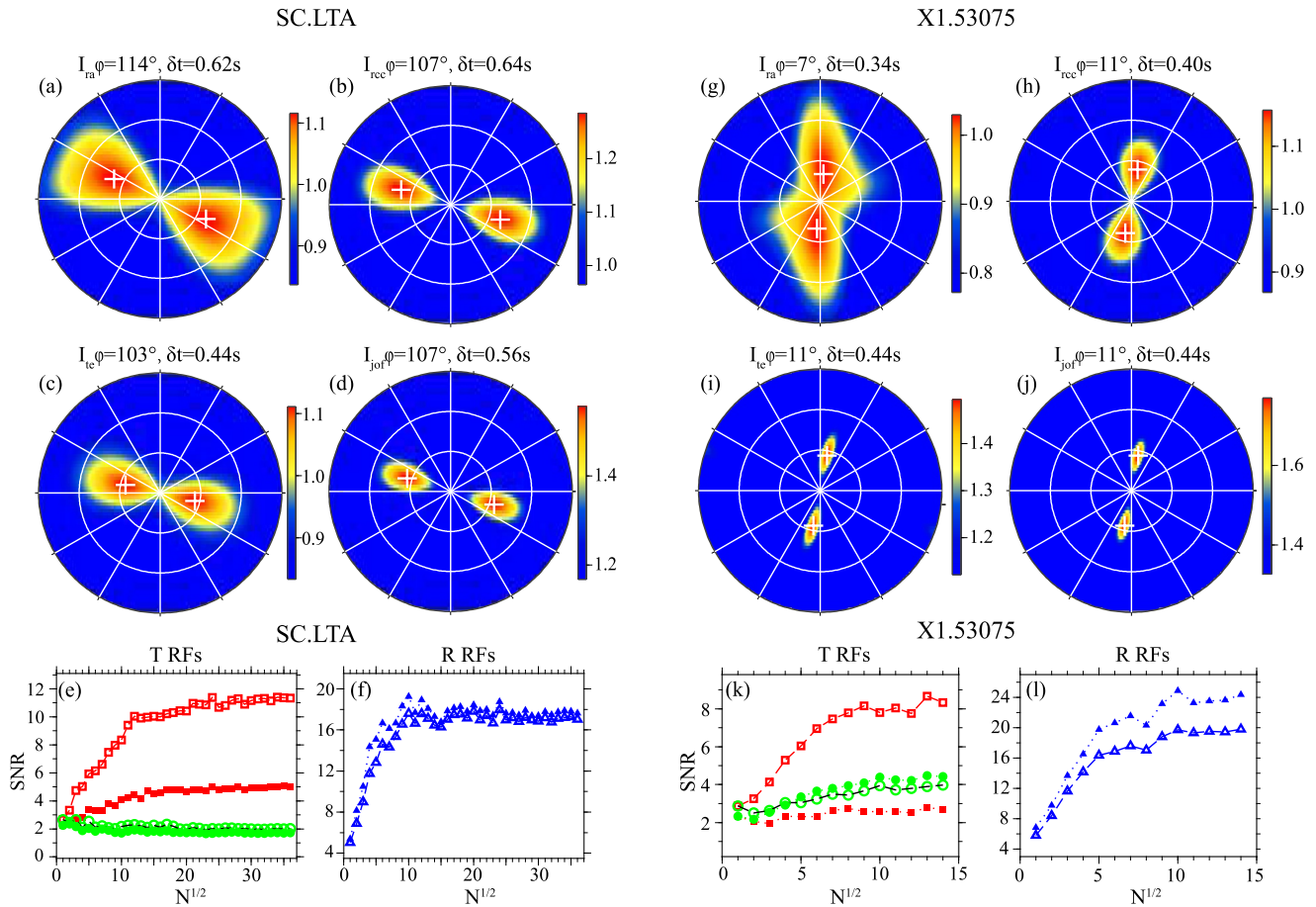


**Figure 5.** Estimates of  $(\varphi, \delta t)$  using R and T receiver functions of SC.LTA based on the three IOFs (a–c) and the JOF (d). In each azimuthal plot, amplitude of the objective function is shown as a function of fast polarization direction (azimuth) and delay time (radius). The peak amplitude is indicated by the white pluses. (e) and (f) shows the results of statistical analyses with T and R receiver functions. Open and filled symbols in (e) and (f) represent SNR calculated from stacks of receiver functions before and after the removal of seismic anisotropy determined by the JOF. Note the steady increase of open square (stack with a sign correction of back azimuth) with increasing  $N^{1/2}$  in (e) and that the filled triangles are generally above the open ones in (f). (g–l) are the same as (a–f) except for station X1.53075.

## 2.5. Estimate of Crustal Anisotropy

HTI anisotropy is often measured with two parameters, fast polarization direction  $\varphi$  and delay time  $\delta t$  between the fast and slow directions, which are obtained through grid search of objective functions. Here, we followed H. Liu and Niu (2012) and employed three individual objective functions (IOFs) to search for a robust pair of  $(\varphi, \delta t)$ . The three IOFs are: (a) the peak energy of the R RFs stacked along a degree-2 harmonic traveltime curve,  $T_{Pms}^{n,i}(\theta_i)$ , where  $n = 2$ ,  $I_{rcos}(\varphi, \delta t)$ ; (b) the cross-correlation of individual R RFs after a full correction of crustal anisotropy,  $I_{rec}(\varphi, \delta t)$ ; (c) total energy of the T RFs after removal of crustal anisotropy,  $I_t(\varphi, \delta t)$ . A joint objective function (JOF) is further calculated through a weighted average of the three IOFs:

$$\ln I(\varphi, \delta t) = w_1 \ln I_{rcos}(\varphi, \delta t) + w_2 \ln I_{rec}(\varphi, \delta t) - w_2 \ln I_t(\varphi, \delta t) \quad (4)$$

Here  $w_1$ ,  $w_2$ , and  $w_3$  are the relative weights of the three IOFs, which can be determined on the basis of the relative confidence level of the three measurements. We set them to one in this study for simplicity. Figure 5 shows the estimated  $(\varphi, \delta t)$  at stations SC.LTA and X1.53075. In general, all the estimates based on the three IOFs and the JOFs are consistent, suggesting a robust representation of azimuthal anisotropy inside the crust beneath these two stations.

We further conducted statistical analysis to verify the reliability of the anisotropy results. The basic principle is that if there is a coherent signal in a targeted window of individual RFs, stacking can lead to an increase of SNR.

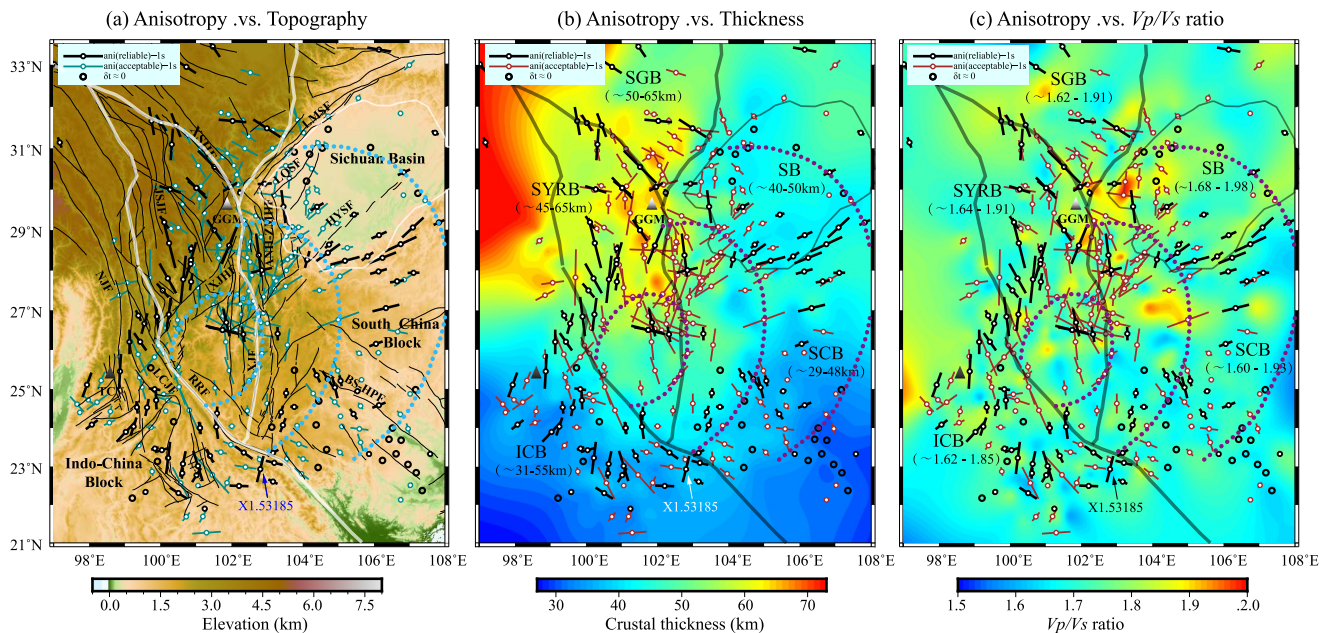


**Figure 6.** Maps showing the surface topography (a), crustal thickness (b) and the lateral variations of the  $V_p/V_s$  ratio (c). Note the large contrast in crustal,  $V_p/V_s$  ratio and splitting time between the SYRB and the rest of the study area. Also shown on the map are the measurements of the fast directions and splitting times. The fast-axis direction is shown by a bar line, and the amount of splitting is indicated by the length of the bar line. The black bar lines are reliable anisotropic results, while the dark cyan (a) and brown (b, c) bar lines are acceptable results. The dotted lines in (b) and (c) indicate the boundaries of the inner, middle, and outer zones of the ELIP (Xu et al., 2004). ANH-ZMHF: Anninghe-Zemuhe Fault; BS-HPF: Baise-Hepu Fault; HYSF: Huayingshan Fault; JSJF: Jinshajiang Fault; LCJF: Lancangjiang Fault; LMSF: Longmenshan Fault; LQSF: Longquanshan Fault; NJF: Nujiang Fault; RRF: Red River Fault; XJF: Xiaojiang Fault; XJHF: Xiaojinhe Fault; XSHF: Xianshuihe Fault; GGM: Gongga Mountain; TCV: Tengchong Volcano.

In other words, if the SNR stay unchanged during the stacking, then the targeted window comprises only noise. We employed the following four principles to verify that azimuthal variations of the  $Pms$  window on the R and T RFs are originated from azimuthal anisotropy: (a) When the uncorrected T RFs are used in stacking, the SNR of stacked RFs remains nearly the same. This is because  $Pms$  has a positive and negative mixed polarity so that stacking becomes destructive, especially when the RFs are evenly distributed in the backazimuth direction (open circles in Figures 5e and 5k). (b) However, after correcting anisotropy induced polarity changes, the SNR of stacked T-RFs increases steadily with number of RFs ( $N$ ) (open squares in Figures 5e and 5k). (c) After correction of seismic anisotropy, the SNR of the stacked T RFs does not change with  $N$  because the  $Pms$  time window of T RFs sampling an isotropic medium consists of random noise. Therefore, stacking does not yield any increase of SNR regardless of whether a polarity correction is applied (filled squares in Figures 5e and 5k) or not (filled circles in Figures 5e and 5k). (d) The SNR of stacked R RFs increases with  $N$ . When crustal anisotropy is corrected, stacking becomes more efficient (filled triangles in Figures 5f and 5l), leading to a higher SNR as compared to that of the uncorrected R RFs (open triangles in Figures 5f and 5l).

### 3. Results

We applied the above  $H-\kappa$  analysis, harmonic decomposition, and azimuthal anisotropy measurements to all the 711 stations. The results are listed in Table S1 in Supporting Information S1. For the convenience of the following discussion, we divided the study region into five areas: the Songpan-Ganzi Block (SGB) in the northwest, the Sichuan Basin (SB) in the northeast, the rest of South China Block (SCB) in the southeast, the Indo-China Block (ICB) in the southwest, and the Sichuan-Yunnan Rhombic Block (SYRB) in the central part (Figure 6a).

#### 3.1. Crustal Thickness and $V_p/V_s$ Ratio

As the robust identification of  $Pms$  is critical in determining crustal structure, we thus paid special attention to ensure that  $Pms$  is not contaminated by other arrivals, such as shallow reverberations. We performed a slant-stacking analysis to ensure that  $Pms$  reaches its peak at a negative slowness as expected (X. Xu et al., 2018). We found that a total of 588 stations (82.7% of the total 711 stations) has a  $Pms$  that satisfied this slowness

requirement. It should be noted that some of the discarded stations did show reasonable ( $H$ ,  $\kappa$ ) results that are consistent with those of the surrounding stations and previous studies (e.g., W. Wang et al., 2017). Most of the discarded 123 stations exhibited  $H$  or  $\kappa$  values that are either too high or too low for a typical crust. Therefore, we excluded all the measurements from the 123 stations in our results.

Previous studies have found that a complicated crustal and Moho structure can lead to unstable ( $H$ ,  $\kappa$ ) stacking (Frassetto et al., 2011; Ogden et al., 2019). We found that the slowness criteria we employed acts as a decent filter to eliminate stations underlain by complicated crustal and Moho structure. We were able to obtain robust ( $H$ ,  $\kappa$ ) results from all the 588 stations. A map view of the individual measurements of crustal thickness ( $H$ ) and  $V_p/V_s$  ratio ( $\kappa$ ) is shown in Figure S1 in Supporting Information S1. We compared our estimates of ( $H$ ,  $\kappa$ ), especially those with relatively high or low  $V_p/V_s$  ratios with results of previous RF studies in the same region (Sun et al., 2012; W. Wang et al., 2017; M. Xu et al., 2020) and found the results are rather consistent. One example is the CEArray station SC.GZA in the SGB, which exhibits a thick crust (58.1 km) and a high  $V_p/V_s$  ratio (1.905). Both values are quite close to (60.5 km, 1.863) and (58.4 km, 1.93) estimated by Sun et al. (2012) and W. Wang et al. (2017), respectively. Examples with low  $V_p/V_s$  ratios are the CHINArray stations T1.KWC02 in the SGB and X1.51011 at the SB with an estimate of ( $H$ ,  $\kappa$ ) of (46.8 km, 1.666) and (43.1 km, 1.658), respectively. Measurements at the two stations by W. Wang et al. (2017) are (48.5 km, 1.65) and (43.1 km, 1.67). The differences here are within our measurement uncertainties.

We further interpolated the 588 measurements of ( $H$ ,  $\kappa$ ) to a meshed grid of  $0.01^\circ \times 0.01^\circ$  and showed the color contours of crustal thickness and  $V_p/V_s$  ratio in Figures 6b and 6c, respectively. It should be noted that results at the edges and corners are extrapolations with little accuracy. We also showed the range of estimated crustal thickness (Figure 6b) and  $V_p/V_s$  ratio (Figure 6c) of each block. The thickness range is  $\sim(50\text{--}65)$  km,  $\sim(40\text{--}50)$  km,  $\sim(29\text{--}48)$  km,  $\sim(31\text{--}55)$  km, and  $\sim(45\text{--}65)$  km for the SGB, SB, SCB, ICB, and SYRB, respectively, while the corresponding variations in  $V_p/V_s$  ratio are  $\sim(1.62\text{--}1.91)$ ,  $\sim(1.68\text{--}1.98)$ ,  $\sim(1.60\text{--}1.93)$ ,  $\sim(1.62\text{--}1.85)$ , and  $\sim(1.64\text{--}1.91)$ . From west to east, crustal thickness decreases rapidly from  $\sim 50$  to 65 km in the SGB to  $\sim 40\text{--}50$  km in the SB. From north to south, crustal thickness gradually thins from  $\sim 65$  km in the SYRB to  $\sim 30$  km in the ICB and SCB.

### 3.2. Crustal Anisotropy

Results of the harmonic analysis, measurements of azimuthal anisotropy with the three IOFs and the JOF, and statistical analysis of SNR of all the 711 stations are listed in Table S2 in Supporting Information S1. We also employed the method of Silver and Chan (1991) to estimate the measurement errors. In general, due to the lower SNR of the Moho converted  $Pms$  wave and complicated crustal structures in the study area, a significant portion of the station failed the statistical and harmonic tests. Measurements of ( $\varphi$ ,  $\delta t$ ) from the individual IOFs and the JOF are inconsistent. Among the 711 stations, we found that 105 stations showed reliable measurements of ( $\varphi$ ,  $\delta t$ ), that is, (a) azimuthal variations in  $Pms$  arrival time is dominant by a degree-2 harmonic wave; (b) the grid search of three IOFs and the JOF yielded consistent results, that is, the disparities between the joint measurements and those of at least one individual are smaller than the associated uncertainties; (c) the original and anisotropy-corrected RFs passed statistical tests of signal and noise. We also found another 183 stations that showed consistent measurements with the IOFs and JOF and partly passed the SNR tests, which are referred to as acceptable stations. Again, consistent measurements mean that the disparities between the joint measurements and those of at least one individual are smaller than the associated uncertainties. We must admit that the retention of certain stations may be subjective, therefore we listed all the results of the 711 stations in Table S2 in Supporting Information S1 and showed them in Figure S2 in Supporting Information S1. For reference, the results for 15 example stations are shown in Figures S4–S18 in Supporting Information S1. In addition to the above two groups of stations, we also identified 26 stations with splitting times close to zero (Figure 6). In total, we have 314 measurements,  $\sim 41.2\%$  of the total 711 stations. Due to the low SNR of  $Pms$  in general and the complicated crustal structure of the study region, it is very challenging to extract robust estimates of azimuthal anisotropy from the data. In order to enhance lateral resolution, we strive to keep the number of measurements as large as possible while ensuring accuracy of each measurement.

Our ( $\varphi$ ,  $\delta t$ ) measurements of the CEArray stations generally agreed well with the results of Sun et al. (2012), however, we have more measurements due to a larger number of RFs used in this study. For the CHINArray stations, we compared our results with two recent studies, Cai et al. (2016) and Peng et al. (2022), and found

consistent results at many stations and moderate differences at some stations. For example, at station X1.53094, our measurement is (43.0°, 0.68 s), very similar to the results of (38°, 0.66 s) from Cai et al. (2016) and (27°, 0.65 s) from Peng et al. (2022). Station X1.53186 shows moderate differences between our measurement, (116°, 0.26 s), and the two studies, (128°, 0.32 s) and (85°, 0.37 s). In Figure S3 in Supporting Information S1, we show measurements of ( $\varphi$ ,  $\delta t$ ) of previous and our studies in the area, offering a comparison of results derived from different studies.

In general, crust beneath the SGB and SYRB at the eastern part of the Tibetan Plateau exhibited strong azimuthal anisotropy. In the SGB area, the fast polarization direction occurs predominantly in the NW-SE direction, roughly parallels to the strike of the Xianshuihe Fault (XSHF) and perpendiculars to the Longmenshan Fault (LMSF), with an average splitting time of  $\sim 0.6$  s. Compared to SGB, the measured fast polarization direction at the SYRB is somewhat more scattered and the splitting time is slightly larger ( $\geq 0.6$  s). The fast polarization direction is primary in the NW-SE direction in the northern part of the block and then rotates clockwise toward the south. Crustal anisotropy in the southwestern SYRB is relatively strong and uniform but starts to disperse at the Red River Fault (RRF). Reliable measurements of crustal anisotropy of the southeastern SYRB are very limited, and acceptable measurements are highly scattered. Most stations near the Gongga Mountain (GGM) and the inner zone of the ELIP failed to pass the statistical tests.

In addition to the SGB and SYRB, the southern part of the SB and northern area of the SCB exhibit a strong and spatially coherent crustal anisotropy with a fast polarization direction of ENE-WSW and a splitting time up to  $\sim 0.7$  s. Crust beneath vast areas in the northern SB and southern SCB has very weak or no azimuthal anisotropy. A weak to moderate anisotropy is observed from stations on the ICB. The measured ( $\varphi$ ,  $\delta t$ ) values are highly scattered and seem to be related to local geological structures. For example, the fast polarization direction estimated from stations around the Tengchong Volcano (TCV) appears to rotate clockwise around the volcano. Stations near the RRF zone shows a fast polarization direction parallel to the fault, except for the CHINArray station X1.53185, which is located at  $\sim 45$  km from the RRF and has a fast polarization direction almost perpendicular to the fault.

#### 4. Discussion

To better understand our results, we showed the measured ( $\varphi$ ,  $\delta t$ ) values with surface GPS motion direction (Zhao et al., 2015) and XKS splitting parameters (Chang et al., 2015; C. Huang & Chang, 2021) in Figure 7a. We further plotted our measurements on an S-wave velocity map at 30 km from Shen et al. (2016) in Figure 7b. In the following discussion, we focus on the ( $\varphi$ ,  $\delta t$ ) measurements at the 5 blocks and their potential causes and implications.

##### 4.1. SGB Is Likely Deformed by Crustal Shortening and Lower Crustal Flow

Almost all the stations on the SGB showed a fast polarization direction of  $\sim$ NW-SE to  $\sim$ WNW-ESE, which aligns with surface GPS motion direction and the XKS fast polarization direction (Figure 7a), as well as the maximum horizontal tensile stress direction. Our measurements agree well with the results of stations located further northern part of the margin (Q. Wang et al., 2016). Based on the low  $V_p/V_s$  ratio and comparison of crustal and lithospheric anisotropy derived from  $Pms$  and XKS data, Q. Wang et al. (2016) concluded that the northeastern margin of the Tibetan Plateau is primarily deformed by pure shear mechanism, that is, vertically coherent shortening associated with the India-Asia collision. Our measurements from the northeastern edge of the block showed similar seismic features, thus we suggest that collision induced crustal shortening is likely the primary deformation mechanism for this part of the margin. Moving to the southeast, stations close to the LMSF zone tend to have a slightly high  $V_p/V_s$  ratio with the fast polarization direction nearly perpendicular to the strike of fault. These seismic characteristics were also observed by Sun et al. (2015), which were interpreted to be caused by a southeastward flow in the lower crust. Our observations are thus consistent with this interpretation.

L. Chen, Gerya, et al. (2013) conducted 2-D numerical simulations and found that the steep topographic relief across the LMS range is maintained by intensive convergence and large rheological contrast between the SGB and SB even without the presence of a partially molten lower crust beneath the margin. R. Xie et al. (2021) concluded from thermochronological studies that the episodic uplift of the eastern Tibetan Plateau during the Cenozoic era was likely the result of a combination of pure shear crustal thickening and melt doming. The intensive convergence is substantiated by geological data gathered from the LMS range and its periphery (Hubbard &

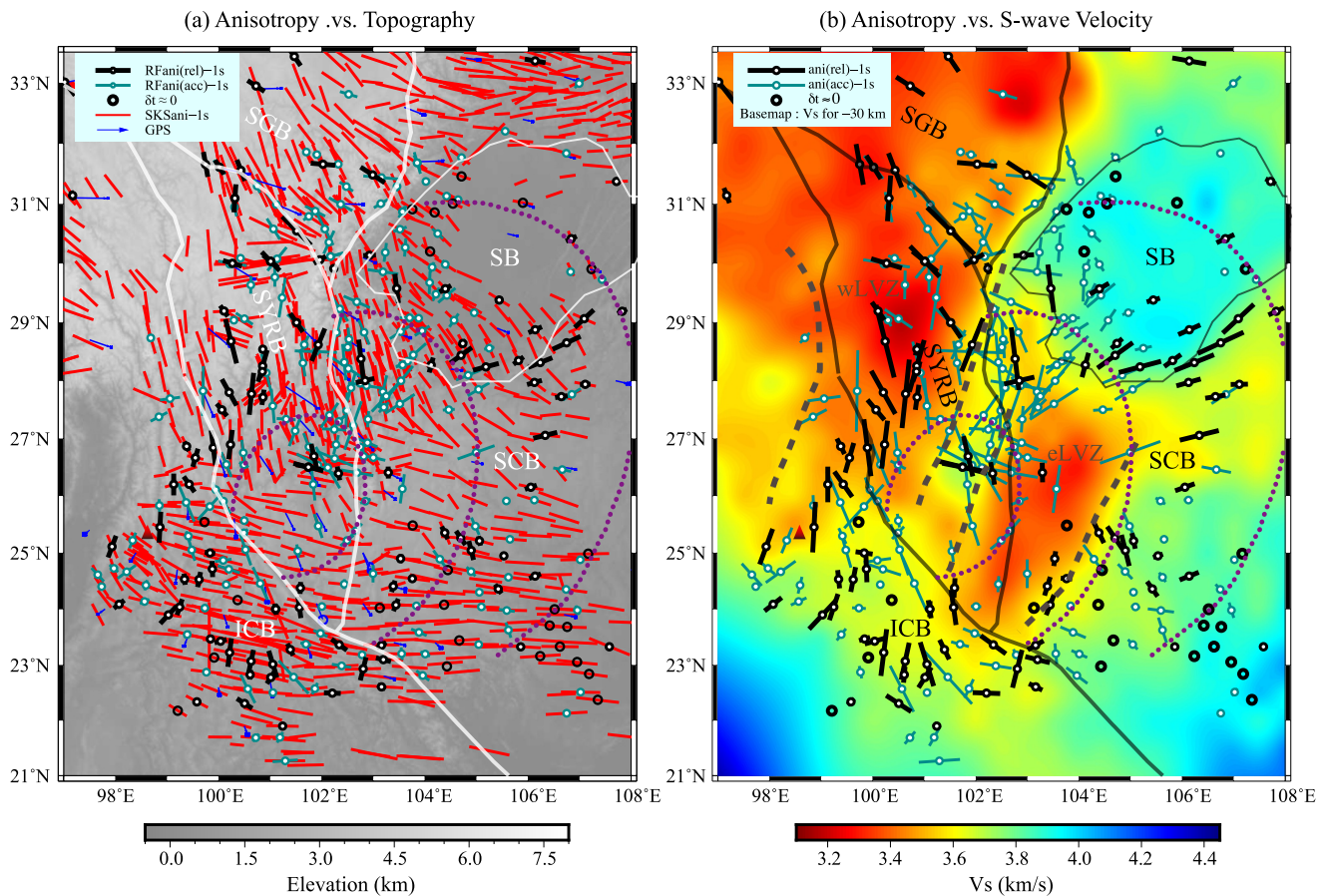


**Figure 7.** The two anisotropic parameters,  $(\varphi, \delta t)$ , measured from the  $Pms$  are shown in black (reliable) and dark cyan (acceptable) bar lines. (a) For comparison, anisotropy from XKS phases (Chang et al., 2015; Huang & Chang, 2021) and GPS velocity (Zhao et al., 2015) are shown in red bar lines and blue arrows, respectively. (b) Comparison to the map of  $V_s$  for 30 km (Shen et al., 2016). Dotted lines in (a) and (b) indicate the boundaries of the inner, middle, and outer zones of the ELIP (Xu et al., 2004). Dashed lines in (b) are boundaries of two channels of LVZs of Bai et al. (2010). Note that the retained anisotropy results are mainly concentrated in the wLVZ, and the direction is consistent with the channel direction of the LVZ. However, in the eLVZ region, only a small number of reliable results have been retained, and the acceptable results are highly scattered, indicating the absence of organized mineral alignment associated with material flow within the eLVZ.

Shaw, 2009), alongside surface wave data (Bao et al., 2020), indicating an azimuthal anisotropy with a fast direction aligned parallel to the strike of the LMS range. Notably, our observations showing a perpendicular fast direction to the strike are primarily situated approximately 80–100 km west of the LMS range, implying potential disparities in crustal deformation behind the range compared to within it. Additionally, we also want to point out that a strike-parallel fast direction in the middle to lower crust could arise from either overall crustal shortening or a redirection of lower crustal flow after encountering significant resistance at the forefront.

#### 4.2. A Diverted Lower Crustal Flow Beneath Northern SYRB

The SYRB region is a key area in the southeastern margin of the Tibetan plateau and is characterized by a highly complex structure with converging subblocks and complicated fault system. Elevation across the SYRB decreases more gradually from the plateau to the foreland as compared to the SGB. As river incision data supported the lower crust flow model for the crustal uplift in this area (Clark et al., 2005), many magnetotelluric and seismic investigations have been conducted to image the lower crustal flow. While magnetotelluric images suggested that high electrical conductivity structures in the lower crust are localized in two continuous channels that run roughly from north to south (Bai et al., 2010), seismic images, on the other hand, showed two distinct LVZs beneath the SYRB and the SCB (e.g., Bao et al., 2015; M. Chen et al., 2014; Y. Liu et al., 2023; Shen et al., 2016; Y. Yang et al., 2020; X. Yang et al., 2023; Zhang et al., 2020). The two LVZs seem to be separated by the inner zone of the ELIP and will be referred to as eLVZ and wLVZ, respectively (Figure 7b). The distinct difference between the south and north is also documented by many shear-wave splitting studies (e.g., Cai et al., 2016; Chang et al., 2015;

Y. Chen, Gerya, et al., 2013; Gao et al., 2020; P. Huang et al., 2022; Y. Li & Gao, 2023; Lev et al., 2006; Peng et al., 2022; Shi et al., 2023), which showed a rapid change in the fast polarization direction at around 26.5°N.

The wLVZ is a large-scale structure that covers the entire northern SYRB with a southward decrease in both topography and Moho depth. This part of the SYRB is featured by a thick crust and a high  $V_p/V_s$  ratio, albeit with a notably patchy distribution in the high  $V_p/V_s$  region. Both observations support a scenario that crustal thickening is likely caused by an addition of mafic lower crustal rocks with high  $V_p/V_s$  ratio (Tarkov & Vavakin, 1982). Given the limited availability of reliable measurements of crustal anisotropy, it remains challenging to accurately delineate the extent of lower crustal flow in the region. The high  $V_p/V_s$  ratio may also indicate that partial melting is present in the lower crust and leads to the observed low S-wave velocity (Watanabe, 1993). Stations above the wLVZ exhibit strong crustal anisotropy with a splitting time greater than 0.6 s and a fast polarization direction of ~N-S to NNW-SSE in the northern part (Figure 7b). Moving to the south, the fast direction seems to rotate clockwise to ~NNE-SSW, roughly parallel to the southern edge of the wLVZ. Seismic anisotropy in the upper crust is generally caused by alignment of cracks, which can only introduce a delay time of ~0.1 s (Crampin & Peacock, 2005; Gao et al., 2008). Therefore, most of the observed large splitting times must be originated from seismic anisotropy in the lower crust. One candidate lower crustal mineral is amphibole, which exhibits a single-crystal anisotropy of ~30% for S-wave (Aleksandrov & Ryzhova, 1961). Recent experimental study (Ko & Jung, 2015) showed that when amphibole is subjected under simple shear the mineral aggregate can produce a fast polarization direction subparallel to the simple shear direction, like the LPO anisotropy of the olivine mineral in the upper mantle. If the observed  $Pms$  splitting is caused by simple shear of amphibole, then the observed fast polarization directions suggest a lower crustal flow beneath the eastern edge of the SYRB, along the XSHF. The flow seems to turn toward southwest when it hits the core of ELIP (Figure 7).

The eLVZ covers the southeastern tip of the SYRB and extends to a large part of SCB (Figure 7b). Unlike the wLVZ, it is featured by a lower  $V_p/V_s$  ratio. The presence of a large area of partial melts in the crust is usually accompanied by an elevated  $V_p/V_s$  ratio; thus, the low  $V_p/V_s$  ratio may suggest that partial melts are not extensively presented within the eLVZ, a likely indication for the lack of lower crustal flow. The  $Pms$  splitting parameters from stations above the eLVZ and the surroundings are very scattered, a feature that was also commonly observed by previous crustal anisotropy studies (e.g., Cai et al., 2016; Han et al., 2020; Peng et al., 2022; T. Zheng et al., 2018). At the northern tip of the eLVZ, we found a few measurements with a ~N-S fast direction near the Anninghe-Zemuhe Fault (ANH-ZMHF) zone. Moving to the south, we have very few reliable measurements within the first and second rims of the ELIP and the Xiaojiang Fault (XJFZ) zone, as most stations did not pass the slowness and statistical tests (Figure 7b). This may suggest that this area has experienced a complicated deformation history, and there is no single dominant mechanism prevailed across the whole area. We have a few measurements at the southeastern edge of the eLVZ, and the measured splitting times are very small. Therefore, the observed crustal anisotropy also disfavors the presence of an organized lower crust flow in the eLVZ area. In fact, all the most recent tomographic studies (e.g., Y. Yang et al., 2020; X. Yang et al., 2023; Zhang et al., 2020) showed that the eLVZ is disconnected from the wLVZ, suggesting that it has a different origin from the wLVZ, such as mantle upwelling (Z. Huang et al., 2015) or crustal thickening and partial melting in the mid-lower crust (Zhang et al., 2020).

### 4.3. Crustal Shortening Beneath Southeastern SB

In addition to the large crustal anisotropy observed beneath the SGB and SYRB, we found that stations located in the southeastern SB shows significant splitting times (~0.3–0.7 s) with a fast polarization direction of ~WSW-ENE. The direction is roughly parallel to the southeastern edge of the basin and perpendicular to the convergence direction at the LMSF between the SB and SGB.  $H-\kappa$  stacking showed that the underlying crust of the stations is slightly thicker (~50 km) than the rest (~40 km) of the SB (Figure 6b) with an average  $V_p/V_s$  ratio of ~1.75. All these observations suggested that crustal shortening might be occurring at the southeastern edge of the SB as a remote response to the SGB-SB convergence.

## 5. Conclusions

We measured crustal thickness,  $V_p/V_s$  ratio, and crustal anisotropy from receiver functions of teleseismic events recorded by a dense array of broadband stations on the eastern margin of the Tibetan Plateau and the surrounding areas. By comparing our results with GPS motion and XKS splitting as well high-resolution velocity models of

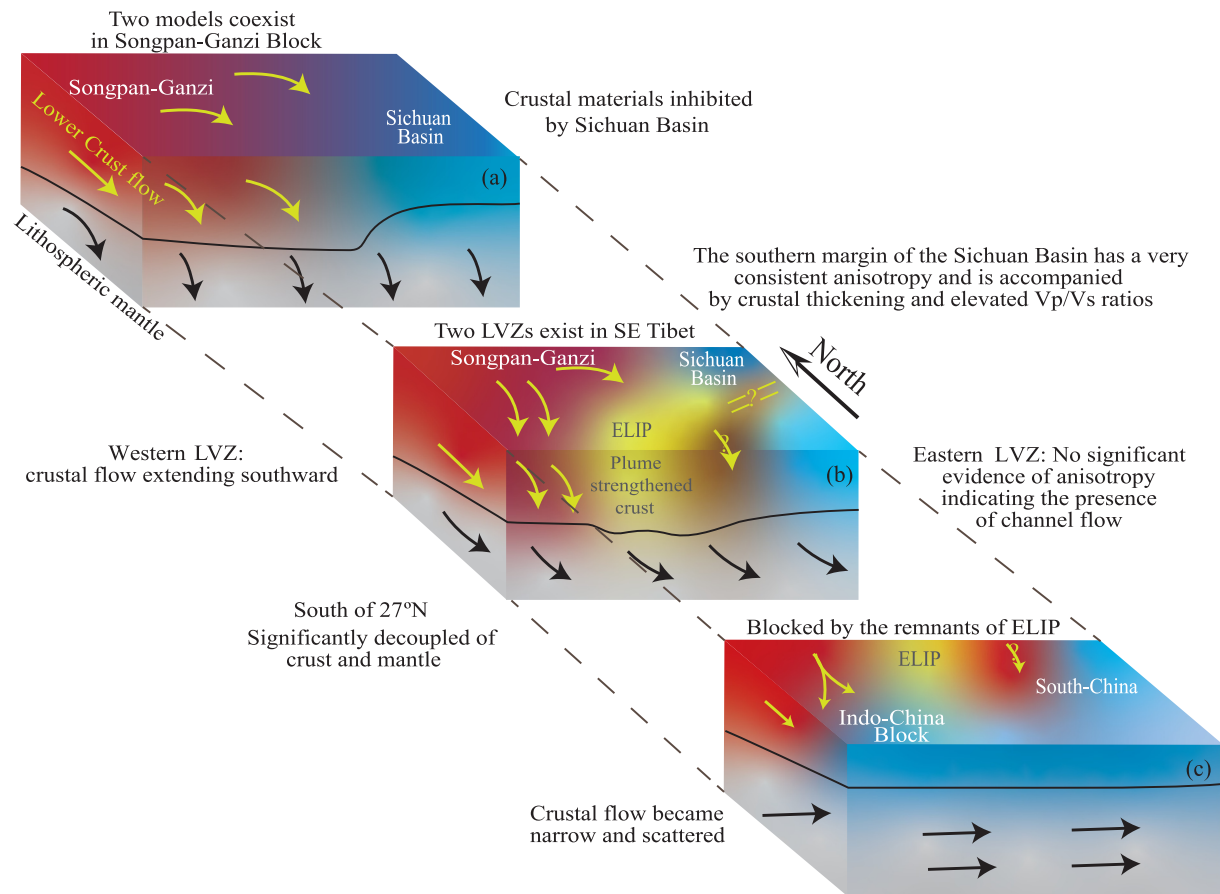


**Figure 8.** Schematic diagrams showing possible mechanisms for crustal deformation and plateau expansion at the eastern margin of the Tibetan Plateau. The black line in the figure depicted the overall Moho relief trend, the yellow arrow indicated the possible movement direction of crustal material, and the black arrow indicated the possible movement direction of mantle material. (a) The SGB is likely deformed by crustal shortening and lower crustal flow. (b) The northern SYRB seems to be uplifted by inflow of lower crustal materials from the central part of the plateau. The ELIP acts as a strong barrier to divert the lower crustal flow and prevents it moving further south. The low S-wave velocity anomaly (eLVZ) in the lower crust beneath the southern SYRB and SCB is unlikely the continuation of the channel flow beneath northern SYRB (wLVZ). (c) Crustal deformation on the southeastern edge of the SB could be the remote response of the convergence between the SB and the Tibetan Plateau.

the study area, we reached the following conclusions (as illustrated in Figure 8): (a) both pure shear (whole crustal shortening) and simple shear (lower crustal flow) played a role for the deformation occurring on the Songpan-Ganzi Block. (b) The northern Sichuan Yunnan Rhombic Block shows a thick crust with a high  $V_p/V_s$  ratio, as well as a large-scale low  $V_s$  in the lower crust, which are consistent with a scenario of southward flow of hot lower crustal materials from the central part of the plateau to the margin. (c) The low velocity anomaly beneath the southeastern Sichuan Yunnan Rhombic Block has a low  $V_p/V_s$  ratio and scattered measurements of  $Pms$  splitting, which can be used to argue against the presence of partial melts and material flow in the lower crust. (d) The southeastern edge of the Sichuan Basin exhibits a deformation pattern consistent with crustal shortening in response to the remote convergence at the Longmenshan Fault zone.

### Data Availability Statement

All the waveform data used in this study are available at (Zeng, 2023). The earthquake catalog was downloaded from the U.S. Geological Survey (USGS, 2024). All the figures were prepared using Generic Mapping Tools (GMT; Wessel et al., 2013).

**Acknowledgments**

We thank the China Seismic Array Data Management Center at the Institute of Geophysics, China Earthquake Administration and the Data Management Centre of the China National Seismic Network at the Institute of Geophysics, China Earthquake Administration for providing the seismic data. The authors are grateful to Can Ge, Yongdong Li, and Muhammad Shahid Riaz for helpful discussions that improved the original manuscript. We also thank the Editor, Dr. Michael Bostock, the Associate Editor, and the reviewers for providing very thoughtful and constructive reviews that improved the manuscript significantly. This work is processed on the high-performance computing platform TS10000 of the School of Geophysics and Geomatics, China University of Geosciences (Wuhan). This work was supported by Open Fund of Hubei Subsurface Multi-Scale Imaging Key Laboratory (No. SMIL-2020-01), NSFC Grants (No. 42274082, 42030108, 41874053), the Open Fund of the Joint Laboratory for High Pressure Physics and Earthquake Science and Technology (No. 2022HPPES06) and the funding for Outstanding Youth Team of Central Universities (No.106-G1323523051).

**References**

Aleksandrov, K., & Ryzhova, T. (1961). The elastic properties of rock forming minerals, pyroxenes, and amphiboles. *Bulletin of the Academy of Sciences of the USSR, Physical Series*, 871(875), 1339–1344.

Bai, D., Unsworth, M. J., Meju, M. A., Ma, X., Teng, J., Kong, X., et al. (2010). Crustal deformation of the eastern Tibetan Plateau revealed by magnetotelluric imaging. *Nature Geoscience*, 3(5), 358–362. <https://doi.org/10.1038/ngeo830>

Bao, X., Song, X., Eaton, D. W., Xu, Y., & Chen, H. (2020). Episodic lithospheric deformation in eastern Tibet inferred from seismic anisotropy. *Geophysical Research Letters*, 47(3), e2019GL085721. <https://doi.org/10.1029/2019GL085721>

Bao, X., Sun, X., Xu, M., Eaton, D. W., Song, X., Wang, L., et al. (2015). Two crustal low-velocity channels beneath SE Tibet revealed by joint inversion of Rayleigh wave dispersion and receiver functions. *Earth and Planetary Science Letters*, 415, 16–24. <https://doi.org/10.1016/j.epsl.2015.01.020>

Cai, Y., Wu, J., Fang, L., Wang, W., & Yi, S. (2016). Crustal anisotropy and deformation of the southeastern margin of the Tibetan Plateau revealed by Pms splitting. *Journal of Asian Earth Sciences*, 121, 120–126. <https://doi.org/10.1016/j.jseas.2016.02.005>

Chang, L., Ding, Z., & Wang, C. (2015). Upper mantle anisotropy beneath the southern segment of North-South tectonic belt, China. *Chinese Journal of Geophysics*, 58(11), 4052–4067. <https://doi.org/10.6038/cjg20151114>

Chen, L., Gerya, T., Zhang, Z., Zhu, G., Duretz, T., & Jacoby, W. R. (2013). Numerical modeling of eastern Tibetan-type margin: Influences of surface processes, lithospheric structure, and crustal rheology. *Gondwana Research*, 24(3–4), 1091–1107. <https://doi.org/10.1016/j.gr.2013.01.003>

Chen, M., Huang, H., Yao, H., van der Hilst, R., & Niu, F. (2014). Low wave speed zones in the crust beneath SE Tibet revealed by ambient noise adjoint tomography. *Geophysical Research Letters*, 41(2), 334–340. <https://doi.org/10.1002/2013gl058476>

Chen, Y., Zhang, Z. J., Sun, C. Q., & Badal, J. (2013). Crustal anisotropy from Moho converted Ps wave splitting analysis and geodynamic implications beneath the eastern margin of Tibet and surrounding regions. *Gondwana Research*, 24(3–4), 946–957. <https://doi.org/10.1016/j.gr.2012.04.003>

Clark, M. K., House, M. A., Royden, L. H., Whipple, K. X., Burchfiel, B. C., Zhang, X., & Tang, W. (2005). Late Cenozoic uplift of southeastern Tibet. *Geology*, 33(6), 525–528. <https://doi.org/10.1130/G21265.1>

Clark, M. K., & Royden, L. H. (2000). Topographic ooze: Building the eastern margin of Tibet by lower crustal flow. *Geology*, 28(8), 703–706. [https://doi.org/10.1130/0091-7613\(2000\)28<703:TOBTEM>2.0.CO;2](https://doi.org/10.1130/0091-7613(2000)28<703:TOBTEM>2.0.CO;2)

Clayton, R. W., & Wiggins, R. A. (1976). Source shape estimation and deconvolution of teleseismic body waves. *Geophysical Journal International*, 47(1), 151–177. <https://doi.org/10.1111/j.1365-246X.1976.tb01267.x>

Crampin, S., & Peacock, S. (2005). A review of shear-wave splitting in the compliant crack-critical anisotropic Earth. *Wave Motion*, 41(1), 59–77. <https://doi.org/10.1016/j.wavemoti.2004.05.006>

England, P., & Houseman, G. (1986). Finite strain calculations of continental deformation: 2. Comparison with the India-Asia collision zone. *Journal of Geophysical Research*, 91(B3), 3664–3676. <https://doi.org/10.1029/JB091iB03p03664>

Frassetto, A. M., Zandt, G., Gilbert, H., Owens, T. J., & Jones, C. H. (2011). Structure of the Sierra Nevada from receiver functions and implications for lithospheric foundering. *Geosphere*, 7(4), 898–921. <https://doi.org/10.1130/ges00570.1>

Gao, Y., Shi, Y., Liang, W., Liu, X., & Hao, P. (2008). Systematic analysis method of shear-wave splitting SAM (2007): Software system. *Earthquake Research in China*, 24(4), 345–353. <https://doi.org/10.3969/j.issn.1001-4683.2008.04.004>

Gao, Y., Shi, Y., & Wang, Q. (2020). Seismic anisotropy in the southeastern margin of the Tibetan Plateau and its deep tectonic significances. *Chinese Journal of Geophysics*, 63(3), 802–816. <https://doi.org/10.6038/cjg202000033>

Han, C., Xu, M., Huang, Z., Wang, L., Xu, M., Mi, N., et al. (2020). Layered crustal anisotropy and deformation in the SE Tibetan plateau revealed by Markov-Chain-Monte-Carlo inversion of receiver functions. *Physics of the Earth and Planetary Interiors*, 306, 106522. <https://doi.org/10.1016/j.pepi.2020.106522>

Hu, F., Wu, F.-Y., Ducea, M. N., Chapman, J. B., & Yang, L. (2022). Does large-scale crustal flow shape the eastern margin of the Tibetan Plateau? Insights from episodic magmatism of Gongga-Zheduo granitic massif. *Geophysical Research Letters*, 49(12), e2022GL098756. <https://doi.org/10.1029/2022GL098756>

Huang, C., & Chang, L. (2021). Reviews on seismic anisotropy based on shear-wave splitting in the Tibetan Plateau. *Reviews of Geophysics and Planetary Physics*, 52(2), 164–181. <https://doi.org/10.16738/j.dqyx.2020-017>

Huang, P., Gao, Y., & Xue, B. (2022). Advances in the deep tectonics and seismic anisotropy of the Lijiang-Xiaojinhe fault zone in the Sichuan-Yunnan Block, Southwestern China. *Earthquake Research Advances*, 2(1), 100116. <https://doi.org/10.1016/j.eqrea.2022.100116>

Huang, Z., Wang, P., Xu, M., Wang, L., Ding, Z., Wu, Y., et al. (2015). Mantle structure and dynamics beneath SE Tibet revealed by new seismic images. *Earth and Planetary Science Letters*, 411, 100–111. <https://doi.org/10.1016/j.epsl.2014.11.040>

Hubbard, J., & Shaw, J. H. (2009). Uplift of the Longmen Shan and Tibetan plateau, and the 2008 Wenchuan (M = 7.9) earthquake. *Nature*, 458(7235), 194–197. <https://doi.org/10.1038/nature07837>

Kennett, B., & Engdahl, E. (1991). Travel times for global earthquake location and phase identification. *Geophysical Journal International*, 105(2), 429–465. <https://doi.org/10.1111/j.1365-246X.1991.tb06724.x>

Ko, B., & Jung, H. (2015). Crystal preferred orientation of an amphibole experimentally deformed by simple shear. *Nature Communications*, 6(1), 6586. <https://doi.org/10.1038/ncomms7586>

Laske, G., Masters, G., Ma, Z., & Pasyanos, M. (2013). Update on CRUST1.0-A 1-degree global model of Earth’s crust. *Geophysical Research Abstracts*, 15, 2658.

Lev, E., Long, M. D., & van der Hilst, R. D. (2006). Seismic anisotropy in Eastern Tibet from shear wave splitting reveals changes in lithospheric deformation. *Earth and Planetary Science Letters*, 251(3–4), 293–304. <https://doi.org/10.1016/j.epsl.2006.09.018>

Levin, V., & Park, J. (1997). P-SH conversions in a flat-layered medium with anisotropy of arbitrary orientation. *Geophysical Journal International*, 131(2), 253–266. <https://doi.org/10.1111/j.1365-246X.1997.tb01220.x>

Li, X., Ma, X., Chen, Y., Xue, S., Varentsov, I. M., & Bai, D. (2020). A plume-modified lithospheric barrier to the southeastward flow of partially molten Tibetan crust inferred from magnetotelluric data. *Earth and Planetary Science Letters*, 548, 116493. <https://doi.org/10.1016/j.epsl.2020.116493>

Li, Y., & Gao, Y. (2023). Rigid widths of active block boundary faults revealed by crustal seismic anisotropy: Examples in the intersection of faults Honghe and Xiaojiang in the SE margin of the Tibetan Plateau. *Geophysical Journal International*, 235(2), 1504–1518. <https://doi.org/10.1093/gji/ggad279>

Liu, H., & Niu, F. (2012). Estimating crustal seismic anisotropy with a joint analysis of radial and transverse receiver function data. *Geophysical Journal International*, 188(1), 144–164. <https://doi.org/10.1111/j.1365-246X.2011.05249.x>



- Liu, Y., Yu, Z., Zhang, Z., Yao, H., Wang, W., Zhang, H., et al. (2023). The high-resolution community velocity model V2.0 of southwest China, constructed by joint body and surface wave tomography of data recorded at temporary dense arrays. *Science China Earth Sciences*, 66(10), 2368–2385. <https://doi.org/10.1007/s11430-022-1161-7>
- Niu, F., Baldwin, T., Pavlis, G., Vernon, F., Rendon, H., Bezada, M., & Levander, A. (2007). Receiver function study of the crustal structure of the Southeastern Caribbean Plate Boundary and Venezuela. *Journal of Geophysical Research*, 112(B11), 308. <https://doi.org/10.1029/2006JB004802>
- Niu, F., & James, D. E. (2002). Fine structure of the lowermost crust beneath the Kaapvaal craton and its implications for crustal formation and evolution. *Earth and Planetary Science Letters*, 200(1–2), 121–130. [https://doi.org/10.1016/S0012-821X\(02\)00584-8](https://doi.org/10.1016/S0012-821X(02)00584-8)
- Niu, F., & Li, J. (2011). Component azimuths of the CEArray stations estimated from P wave particle motion. *Earthquake Science*, 24(1), 3–13. <https://doi.org/10.1007/s11589-011-0764-8>
- Ogden, C. S., Bastow, I. D., Gilligan, A., & Rondenay, S. (2019). A reappraisal of the H- $\kappa$  stacking technique: Implications for global crustal structure. *Geophysical Journal International*, 219(3), 1491–1513. <https://doi.org/10.1093/gji/ggz364>
- Peng, H., Gao, Z., Hu, J., Yang, H., Badal, J., Chen, M., & Zhang, T. (2022). Upper mantle anisotropy in the southeastern margin of the Tibetan Plateau and geodynamic implications. *Physics of the Earth and Planetary Interiors*, 327, 106877. <https://doi.org/10.1016/j.pepi.2022.106877>
- Savage, M. K. (1998). Lower crustal anisotropy or dipping boundaries? Effects on receiver functions and a case study in New Zealand. *Journal of Geophysical Research*, 103(B7), 15069–15087. <https://doi.org/10.1029/98jb00795>
- Shen, W., Ritzwoller, M. H., Kang, D., Kim, Y. H., Lin, F.-C., Ning, J., et al. (2016). A seismic reference model for the crust and uppermost mantle beneath China from surface wave dispersion. *Geophysical Journal International*, 206(2), 954–979. <https://doi.org/10.1093/gji/ggw175>
- Shi, Y., Gao, Y., Zhang, H., Zhang, Z., & Li, G. (2023). Crustal azimuthal anisotropy in the lateral collision zone of the SE margin of the Tibetan Plateau and its tectonic implications. *Geophysical Journal International*, 234(1), 1–11. <https://doi.org/10.1093/gji/ggad059>
- Silver, P. G., & Chan, W. W. (1991). Shear wave splitting and subcontinental mantle deformation. *Journal of Geophysical Research*, 96(B10), 16429–16454. <https://doi.org/10.1029/91JB00889>
- Sun, Y., Liu, J., Zhou, K., Chen, B., & Guo, R. (2015). Crustal structure and deformation under the Longmenshan and its surroundings revealed by receiver function data. *Physics of the Earth and Planetary Interiors*, 244, 11–22. <https://doi.org/10.1016/j.pepi.2015.04.005>
- Sun, Y., Niu, F., Liu, H., Chen, Y., & Liu, J. (2012). Crustal structure and deformation of the SE Tibetan Plateau revealed by receiver function data. *Earth and Planetary Science Letters*, 349, 186–197. <https://doi.org/10.1016/j.epsl.2012.07.007>
- Tapponnier, P., Lacassin, R., Leloup, P. H., Scharer, U., Zhong, D., Wu, H., et al. (1990). The Ailao Shan/Red River metamorphic belt: Tertiary left-lateral shear between Indochina and South China. *Nature*, 343(6257), 431–437. <https://doi.org/10.1038/343431a0>
- Tapponnier, P., Peltzer, G., Le Dain, A. Y., Armijo, R., & Cobbold, P. (1982). Propagating extrusion tectonics in Asia: New insights from simple experiments with plasticize. *Geology*, 10(12), 611–616. [https://doi.org/10.1130/0091-7613\(1982\)10<611:PETIAN>2.0.CO;2](https://doi.org/10.1130/0091-7613(1982)10<611:PETIAN>2.0.CO;2)
- Tarkov, A. P., & Vavakin, V. V. (1982). Poisson's ratio behavior in crystalline rocks: Application to the study of the Earth's interior. *Physics of the Earth and Planetary Interiors*, 29(1), 24–29. [https://doi.org/10.1016/0031-9201\(82\)90134-0](https://doi.org/10.1016/0031-9201(82)90134-0)
- U.S. Geological Survey. (2024). Latest earthquakes [Dataset]. Retrieved from <https://www.usgs.gov/programs/earthquake-hazards/earthquakes>
- Wang, C., Chan, W. W., & Mooney, W. D. (2003). Three-dimensional velocity structure of crust and upper mantle in southwestern China and its tectonic implications. *Journal of Geophysical Research*, 108(B9), 2442. <https://doi.org/10.1029/2002JB001973>
- Wang, Q., Niu, F., Gao, Y., & Chen, Y. (2016). Crustal structure and deformation beneath the NE margin of the Tibetan plateau constrained by teleseismic receiver function data. *Geophysical Journal International*, 204(1), 167–179. <https://doi.org/10.1093/gji/ggv420>
- Wang, W., Wu, J., Fang, L., Lai, G., & Cai, Y. (2017). Crustal thickness and Poisson's ratio in southwest China based on data from dense seismic arrays. *Journal of Geophysical Research: Solid Earth*, 122(9), 7219–7235. <https://doi.org/10.1002/2017JB013978>
- Watanabe, T. (1993). Effects of water and melt on seismic velocities and their application to characterization of seismic reflectors. *Geophysical Research Letters*, 20(24), 2933–2936. <https://doi.org/10.1029/93gl03170>
- Wessel, P., Smith, W. H., Scharroo, R., Luis, J., & Wobbe, F. (2013). Generic mapping tools: Improved version released. *Eos, Transactions, American Geophysical Union*, 94(45), 409–410. <https://doi.org/10.1002/2013EO450001>
- Xie, J., Ritzwoller, M. H., Shen, W., & Wang, W. (2017). Crustal anisotropy across eastern Tibet and surroundings modeled as a depth dependent tilted hexagonally symmetric medium. *Geophysical Journal International*, 209, 466–491. <https://doi.org/10.1093/gji/ggx004>
- Xie, R., Chen, L., Xiong, X., Wang, K., & Yan, Z. (2021). The role of pre-existing crustal weaknesses in the uplift of the eastern Tibetan Plateau: 2D thermomechanical modeling. *Tectonics*, 40(4), e2020TC006444. <https://doi.org/10.1029/2020TC006444>
- Xu, M., Huang, Z., Wang, L., Xu, M., Zhang, Y., Mi, N., et al. (2020). Sharp lateral Moho variations across the SE Tibetan margin and their implications for plateau growth. *Journal of Geophysical Research: Solid Earth*, 125(5), e2019JB018117. <https://doi.org/10.1029/2019JB018117>
- Xu, X., Niu, F., Ding, Z., & Chen, Q. (2018). Complicated crustal deformation beneath the NE margin of the Tibetan plateau and its adjacent areas revealed by multi-station receiver-function gathering. *Earth and Planetary Science Letters*, 497, 204–216. <https://doi.org/10.1016/j.epsl.2018.06.010>
- Xu, Y., He, B., Chung, S., Menzies, M. A., & Frey, F. A. (2004). Geologic, geochemical, and geophysical consequences of plume involvement in the Emeishan flood-basalt province. *Geology*, 32(10), 917–920. <https://doi.org/10.1130/G20602.1>
- Yang, X., Luo, Y., Jiang, C., Yang, Y., Niu, F., & Li, G. (2023). Crustal and upper mantle velocity structure of SE Tibet from joint inversion of Rayleigh wave phase velocity and teleseismic body wave data. *Journal of Geophysical Research: Solid Earth*, 128(7), e2022JB026162. <https://doi.org/10.1029/2022JB026162>
- Yang, Y., Hu, S., Yao, H., Fang, L., & Wu, J. (2020). Crustal shear wave velocity and radial anisotropy in the Xiaojiang fault zone system (SE Tibet) revealed by ambient noise interferometry. *Tectonophysics*, 792, 228594. <https://doi.org/10.1016/j.tecto.2020.228594>
- Yin, A., & Harrison, T. M. (2000). Geologic evolution of the Himalayan-Tibetan orogen. *Annual Review of Earth and Planetary Sciences*, 28(1), 211–280. <https://doi.org/10.1146/annurev.earth.28.1.211>
- Zeng, S. (2023). Data presented in Crustal structure and anisotropy measured by CHINArray and implications for complicated deformation mechanisms beneath the eastern Tibetan margin [Dataset]. *Zenodo*. <https://doi.org/10.5281/zenodo.10156342>
- Zeng, S., Zheng, Y., Niu, F., & Ai, S. (2020). Measurements of seismometer orientation of the first phase CHINArray and their implications on vector-recording-based seismic studies. *Bulletin of the Seismological Society of America*, 111(1), 36–49. <https://doi.org/10.1785/0120200129>
- Zhang, Z., Yao, H., & Yang, Y. (2020). Shear wave velocity structure of the crust and upper mantle in Southeastern Tibet and its geodynamic implications. *Science China Earth Sciences*, 63(9), 1278–1293. <https://doi.org/10.1007/s11430-020-9625-3>
- Zhao, B., Huang, Y., Zhang, C., Wang, W., Tan, K., & Du, R. (2015). Crustal deformation on the Chinese mainland during 1998–2004 based on GPS data. *Geodesy and Geodynamics*, 6(1), 7–15. <https://doi.org/10.1016/j.geog.2014.12.006>
- Zhao, L., Xie, X., He, J., Tian, X., & Yao, Z. (2013). Crustal flow pattern beneath the Tibetan Plateau constrained by regional Lg-wave Q tomography. *Earth and Planetary Science Letters*, 383, 113–122. <https://doi.org/10.1016/j.epsl.2013.09.038>

- Zheng, T., Ding, Z., Ning, J., Chang, L., Wang, X., Kong, F., et al. (2018). Crustal azimuthal anisotropy beneath the southeastern Tibetan Plateau and its geodynamic implications. *Journal of Geophysical Research: Solid Earth*, 123(11), 9733–9749. <https://doi.org/10.1029/2018JB015995>
- Zheng, X., Ouyang, B., Zhang, D., Yao, Z., Liang, J., & Zheng, J. (2009). Technical system construction of data backup centre for China seismograph network and the data support to researches on the Wenchuan earthquake. *Chinese Journal of Geophysics*, 52(5), 412–417. <https://doi.org/10.3969/j.issn.0001-5733.2009.05.031>